Frontiers of Information Technology & Electronic Engineering
www.jzus.zju.edu.cn; engineering.cae.cn; www.springerlink.com
ISSN 2095-9184 (print); ISSN 2095-9230 (online)
E-mail: jzus@zju.edu.cn

Spacecraft damage infrared detection algorithm for hypervelocity impact based on double-layer multi-target segmentation*

Xiao YANG[1], Chun YIN[†‡1], Sara DADRAS[2], Guangyu LEI[1], Xutong TAN[1], Gen QIU[1]

[1]*School of Automation Engineering, University of Electronic Science and Technology of China, Chengdu 611731, China*

[2]*Electrical and Computer Engineering Department, Utah State University, UT 84321, USA*

[†]E-mail: yinchun.86416@163.com; chunyin@uestc.edu.cn

Received Dec. 12, 2020; Revision accepted June 28, 2021; Crosschecked Nov. 22, 2021

Abstract: To detect spacecraft damage caused by hypervelocity impact, we propose an advanced spacecraft defect extraction algorithm based on infrared imaging detection. The Gaussian mixture model (GMM) is used to classify the temperature change characteristics in the sampled data of the infrared video stream and reconstruct the image to obtain the infrared reconstructed image (IRRI) reflecting the defect characteristics. The designed segmentation objective function is used to ensure the effectiveness of image segmentation results for noise removal and detail preservation, while taking into account the complexity of IRRI (that is, the required trade-offs are different). A multi-objective optimization algorithm is introduced to achieve balance between detail preservation and noise removal, and a multi-objective evolutionary algorithm based on decomposition (MOEA/D) is used for optimization to ensure damage segmentation accuracy. Experimental results verify the effectiveness of the proposed algorithm.

Key words: Hypervelocity impact damage; Defect detection; Gaussian mixture model; Image segmentation
https://doi.org/10.1631/FITEE.2000695 **CLC number:** TP391.4

1 Introduction

It is well known that there is a large amount of debris in space (Lamb, 2018; Adushkin et al., 2020; Murtaza et al., 2020). With the systematic development of human space activities, the amount will continue to increase sharply. The harm it causes to spacecraft in hypervelocity collisions seriously threatens on-orbit operation, reusability, and safety of the spacecraft (Aglietti et al., 2020; Huang et al., 2020). The research object in this study is a repeatable spacecraft. When it collides with space debris at an average speed of 10 km/s, the hypervelocity impact causes multiple types of damage to the surface, subsurface, and interior of the spacecraft (Gurtin and Francis, 1981), and the energy and heat generated in the process will melt part of the material to varying degrees, forming more and more complicated spacecraft impact damage situations (Schonberg, 2009; Ciampa et al., 2018), as shown in Fig. 1. Infrared thermal imaging technology (Florez-Ospina and Benitez, 2014; Bossi and Georgeson, 2018) has the in situ, high speed characteristics to meet the needs of repeatable spacecraft defect detection (Maldague, 2001; Veidt and Liew, 2013) of barely visible impact damages (BVID) (Garnier et al., 2011) to aircraft wings, and cracks and delamination in aerospace composite materials (Meola et al., 2015). It has also achieved good detection

‡ Corresponding author

* Project supported by the National Natural Science Foundation of China (No. 61873305) and the Applied Basic Research Program of Sichuan Province, China (Nos. 2018JY0410 and 2019YJ0199)

ORCID: Chun YIN, https://orcid.org/0000-0002-2852-6982

results and is cost-effective.

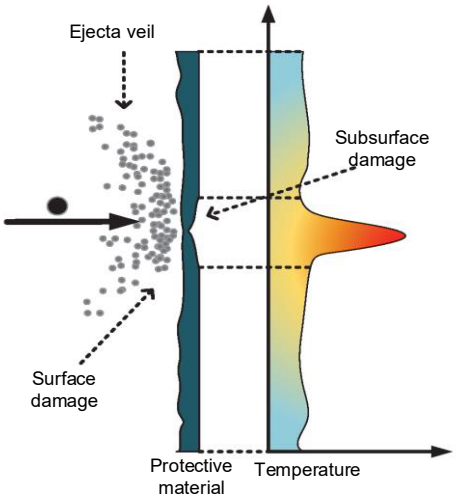

Fig. 1 Schematic of hypervelocity impact damage

The fuzzy C-means (FCM) algorithm (Hossain and Chen, 2019) and its improved algorithm (Namburu et al., 2017) have achieved certain results in image segmentation. Gharnali and Alipour (2018) proposed magnetic resonance imaging (MRI) image segmentation based on nuclear-induced FCM. Vaibhavi and Rupal (2018) proposed a new FCM clustering method based on K-means. However, these segmentation problems are often oriented to a damage function, that is, an objective function that cannot meet the corresponding detection requirements at the same time (Xu et al., 2020).

The defect detection rate will be improved to a certain extent when details are preserved, but the noise is also retained, which will cause incorrect defect recognition and increase the false detection rate. However, if only the overall denoising of the image is achieved, for the damage pattern caused by space debris impact, such as the scattered pits and the small impact points (Fig. 2) distributed around them (Cheng et al., 2018), the defects similar to the noise will be removed along with the denoising. The removal of noise during the denoising process reduces the defect detection rate, which will cause incorrect defect assessment and pose a significant threat to the safety of the spacecraft (Liu et al., 2017).

To improve spacecraft damage detection, retain details, and remove noise interference, we propose a novel multi-objective optimization damage detection algorithm for spacecraft hypervelocity impact evaluation. The algorithm is designed for data processing of a damage detection infrared video stream to obtain an infrared reconstructed image (IRRI) using the transient thermal response (TTR) curve. We also propose a defect segmentation algorithm that achieves the best noise suppression and the best details of IRRI through multi-objective optimization. In the segmentation process, the detailed information of the damaged area should be segmented from the material background area as much as possible to ensure complete defect detection. Simultaneously, it is correctly divided into noise areas to ensure the accuracy of damage detection.

Fig. 2 Hypervelocity impact damage (https://orbitaldebris.jsc.nasa.gov/)

2 IRRI segmentation method based on two-layer multiple targets

2.1 FCM segmentation algorithm

According to Biju and Mythili (2015), FCM is often used in medical image segmentation such as computed tomography (CT) and MRI, and some researchers have used it for microarray image segmentation. The objective function of the FCM image segmentation algorithm is defined as follows:

$$J_{\mathrm{FCM}} = \sum_{i=1}^{MN} \sum_{k=1}^{c} u_{ki}^{m} \|x_i - v_k\|^2, \tag{1}$$

where x_i is the gray value of pixel i, $i = 1, 2, ..., MN$, M and N represent the numbers of pixels corresponding to the length and width of the image, respectively, c is the number of clusters, and m is the value of fuzzification, usually set to 2. The algorithm has the following constraints: $u_{ki} \in$

$[0,1]$, $\sum_{k=1}^{c} u_{ki}=1$. After the iteration is completed, all pixels are classified according to the principle of maximum membership to complete the segmentation of the entire image.

2.2 IRRI segmentation objective function

Although the FCM algorithm can effectively deal with fuzzy problems such as partial volume effects, it still has some flaws. Because the FCM segmentation algorithm ignores the local spatial characteristics of the segmented object, and only the gray value of the pixel is considered, the segmentation result is easily affected by noise. The traditional FCM algorithm has an ideal processing effect only for noise-free images. To solve this problem, the FCM_S algorithm adds a neighborhood item to introduce the neighborhood information of the image space. The corresponding objective function is $f_{\mathrm{FCM\_S}}(\nu)=\sum_{i=1}^{MN}\sum_{t=1}^{c} u_{ti}^{m}[\|x_i-v_t\|^2+\frac{\beta}{N_s}\sum_{j\in N_i}\|x_j-v_t\|^2]$, where N_i is the number of pixels of the i^{th} pixel in the N_s neighborhood window, and β is the number of neighborhood points, a parameter controlling the neighborhood items. However, the IRRI of the segmented object in this study (Fig. 3) has significant problems caused by the noise interference of the imaging link, the detection environment, and the interference of material surface impurity. The blurred edge contour of the impact damage will affect the quantitative results. Therefore, traditional FCM and FCM_S cannot meet the segmentation needs of the experimental objects in this study.

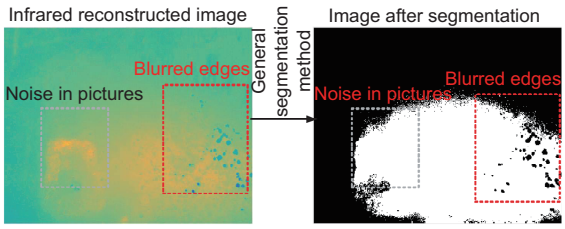

Fig. 3 Multi-objective optimization for image segmentation purposes. References to color refer to the online version of this figure

As shown in Fig. 4, for denoising and preserving detail segmentation for multiple different IRRIs, the comprehensiveness and accuracy of damage detection are ensured. The IRRI segmentation algorithm based on multi-objective optimization proposed in this study establishes an objective function for the two problems that need to be solved, and applies the multi-objective theory to complete image segmentation.

2.2.1 Double-layer multi-objective function construction

It is necessary to perform noise removal and contour detail extraction in IRRI. The segmentation objective function is merged as follows:

$$\min f_3(v)=f_1(v)+f_2(v), \tag{2}$$

where $f_1(v)$ is the edge detail preservation objective function and $f_2(v)$ is the noise elimination objective function. These two functions will affect each other: while suppressing the noise, the details of the defect will be reduced; when the details are maintained, the noise information will be preserved. So, we make the following improvements using the relationship between the two objective functions to adjust the weights:

$$\min f_3(v)=\omega_1^q\cdot f_1(v)+\omega_2^q\cdot f_2(v), \tag{3}$$

where ω_1^q and ω_2^q are the weights corresponding to the objective functions $f_1(v)$ and $f_2(v)$, respectively. $f_1(v)$ and $f_2(v)$ are introduced in the following.

2.2.2 Detail preservation function $f_1(v)$

The impact damage infrared image detail preservation function (DEPF) $f_1(v)$ is constructed to realize the segmentation of image pixel detail information. When constructing $f_1(v)$, the closeness measure $\mathrm{Com}(X,v)$ and departure measure $\mathrm{Sep}(v)$ are considered at the same time, and the ratio of $\mathrm{Com}(X,v)$ to $\mathrm{Sep}(v)$ is expected to be as small as possible to ensure that the detailed information of the infrared image segmentation result of the impact damage is fully retained. Function $f_1(v)$ is defined as

$$f_1(v)=\frac{\mathrm{Com}(X,v)}{\mathrm{Sep}(v)}. \tag{4}$$

In Eq. (4), the closeness measure $\mathrm{Com}(X,v)$ corresponds to the degree of dispersion, and the departure measure $\mathrm{Sep}(v)$ represents the difference of the corresponding pixels. The concepts of compactness and separation come from the literature (Bandyopadhyay et al., 2007; Maulik and Sarkar, 2012)

using the fuzzy clustering index Xie-Beni (XB) proposed by Xie and Beni (1991), to guide the classification of image pixels and realize image segmentation. The idea of establishing the XB index is to complete image classification through the ratio of compactness to separation. When $f_1(v)$ has the minimum value, the defect information of the IRRI itself has the best degree of preservation of detail information.

$$\mathrm{Com}(X,v)=\sum_{t=1}^{c}\frac{\sum_{i=1}^{MN}u_{ti}^{m}\cdot M(x_i,v_t)}{\sum_{i=1}^{MN}u_{ti}}, \quad (5)$$

where $M(x_i,v_t)=\|x_i-v_t\|^2+\alpha_1\|\delta_i-v_t\|^2+\alpha_2\|\tau_i-v_t\|^2$.

In defining the degree of compactness, the complementary effect of local spatial information and non-local spatial information in the pixel space is used to suppress the noise. In Eq. (5), v_t is the clustering center, and the membership of the i^{th} pixel to the k^{th} clustering core is denoted by u_{ti}. Here $u_{ti}=\left(\sum_{p=1}^{c}\left(\frac{\|x_i-c_t\|^2+\alpha_1\|\delta_i-c_t\|^2+\alpha_2\|\tau_i-c_t\|^2}{\|x_i-c_p\|^2+\alpha_1\|\delta_i-c_p\|^2+\alpha_2\|\tau_i-c_p\|^2}\right)^{\frac{1}{m-1}}\right)^{-1}$, and α_1 and α_2 are weighting factors that control Info and NL-Info, respectively. Info δ_i is $\delta_i=\frac{1}{|N_i|}\sum_{a\in N_i}x_a$, where a set N_i is formed by the pixels in the neighborhood window based on pixel i, and x_a is the a^{th} pixel in N_i. NL-Info τ_i is $\tau_i=\sum_{j\in S_i^p}\rho_{ij}x_j$, where S_i^p is a search window of size $p\times p$ centered on the i^{th} pixel, and the weight $\rho_{ij}\,(j\in S_i^p)$ is determined by the similarity of the i^{th} and j^{th} pixels, satisfying $0\le\rho_{ij}\le 1$, $\sum_{j\in S_i^p}\rho_{ij}=1$. The weight is defined as $\rho_{ij}=\frac{1}{\eta_i}\exp(-\left\|\varphi(N_i^{\mathrm{s}})-\varphi(N_j^{\mathrm{s}})\right\|_{2,\alpha}^2/\psi^2)$, where

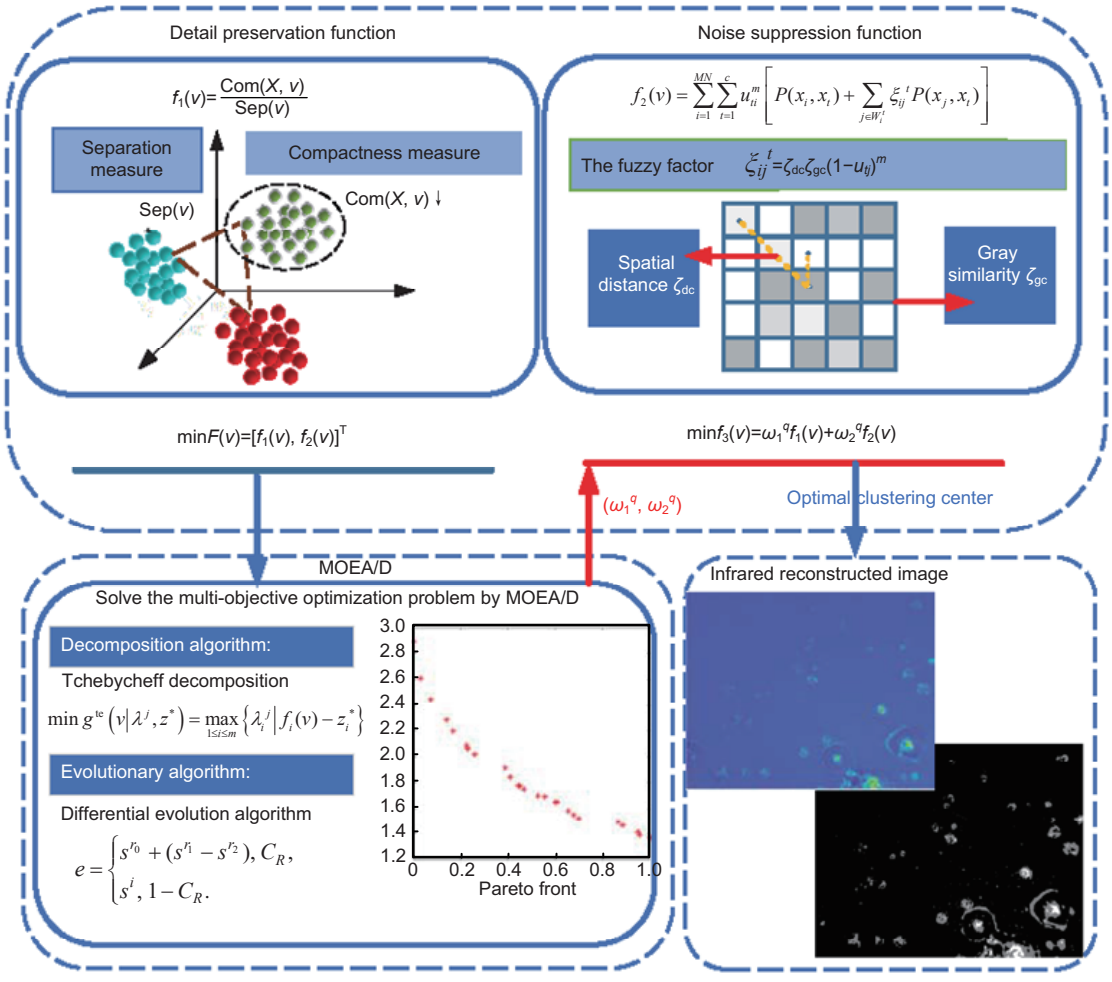

Fig. 4 Image segmentation method based on the multi-objective problem

$\varphi(N_i^s)$ represents the gray vector on the similar window, and ψ is the filtering degree parameter.

The Gaussian weighted Euclidean distance $\left\|\varphi(N_i^s)-\varphi\left(N_j^s\right)\right\|_{2,\alpha}^2$ is used to measure the similarity between the center pixel x_i and the neighboring pixel x_j, and $\eta_i=\sum_{j\in S_i^p}\exp\left(-\frac{\left\|\varphi(N_i^s)-\varphi\left(N_j^s\right)\right\|_{2,\alpha}^2}{\psi^2}\right)$ is an institutionalization term. When defining the global separation function of pixels, distance is used to indicate the degree of dispersion between classes, so there is $\mathrm{Sep}(v)=\sum_{p=1}^{c}\sum_{q=1}^{c}u_{pq}^m\|v_q-v_p\|$, where $u_{pq}=\left[\left(\sum_{l=1,l\neq q}^{c}\frac{\|v_q-v_p\|}{\|v_q-v_l\|}\right)^{\frac{1}{m-1}}\right]^{-1}$ $(p\neq q)$ is the membership of clustering center v_p to v_q.

2.2.3 Noise suppression function $f_2(v)$

To improve the noisy image segmentation, Krinidis and Chatzis (2010) proposed fuzzy local information C-means clustering (FLICM), which uses spatial information of neighboring pixels to define a fuzzy factor. The objective function is

$$f_{\mathrm{FLICM}}(v)=\sum_{i=1}^{MN}\sum_{k=1}^{c}u_{ki}^m\|x_i-v_k\|^2+U_{\mathrm{FLICM}},\quad(6)$$

where

$$U_{\mathrm{FLICM}}=\sum_{j\in N_i}\zeta_{\mathrm{sd}}(1-\mu_{kj})\|x_j-v_k\|.\quad(7)$$

In the FLICM algorithm, the spatial distance of the fuzzy factor is used to measure the influence degree of the neighboring pixels. However, using only the spatial distance cannot accurately measure the neighborhood points or the influence of the neighborhood points on the center point. To resolve the above problem, this paper refers to the construction of the noise suppression function (NOSF) based on the kernel-based fuzzy C-means (KFCM) algorithm proposed by Wu et al. (2003), which has ideal segmentation effect for non-linear clusterable pixels. For the construction of NOSF $f_2(v)$, a new weighted fuzzy term $\sum_{j\in W_i^r}\xi_{ij}^tP(x_j,v_t)$ is introduced in the objective function $f_{\mathrm{KFCM}}(v)=\sum_{i=1}^{MN}\sum_{t=1}^{c}u_{ti}^mP(x_i,v_t)$. The expression of $f_2(v)$ is as follows:

$$f_2(v)=\sum_{i=1}^{MN}\sum_{t=1}^{c}u_{ti}^m\left[P(x_i,v_t)+\sum_{j\in W_i^r}\xi_{ij}^tP(x_j,v_t)\right].\quad(8)$$

In Eq. (8), W_i^r represents the neighborhood search window, $m\in[1,\infty)$ is the smoothing parameter, and $P(x_i,v_t)=1-\exp\left(-\frac{\|x_i-v_t\|^2}{\varepsilon}\right)$ represents the Gaussian radial basis similarity between pixels. ε is a scalar parameter which fully considers the inherent structure of the pixel data itself and satisfies the following equation: $\xi_{ij}^t=\zeta_{\mathrm{dc}}\cdot\zeta_{\mathrm{gc}}\cdot(1-u_{tj})^m$.

In the weighted fuzzy term, the fuzzy factor ζ_{ij} considers both the spatial distance constraint relationship ζ_{dc} and the gray-level constraint relationship ζ_{gc} between the pixels in the neighborhood window. $f_2(v)$ uses the neighborhood information adjustment constraints to reduce the influence of noise pixels on infrared image segmentation. The spatial distance constraint ζ_{dc} satisfies $\zeta_{\mathrm{dc}}=\frac{1}{d_{ij}+1}$.

The spatial gray constraint ζ_{gc} satisfies

$$\zeta_{\mathrm{gc}}=\begin{cases}2+\frac{\varepsilon_{ij}}{\sum_{p\in W_i^r}\varepsilon_{ip}}, & D_j<\overline{D},\\ 2-\frac{\varepsilon_{ij}}{\sum_{p\in W_i^r}\varepsilon_{ip}}, & D_j\geq\overline{D},\end{cases}$$

where $D_j=\frac{\mathrm{Var}(Y_i)}{[\mathrm{Mean}(Y_i)]^2}$ is the ratio of the variance to the mean square of all pixel points Y_i in the r neighborhood of pixel x_j, and $\overline{D}=\sum_{j\in W_i^r}D_j/r^2$. ε_{ij} is the value projected in the kernel space of the mean square error of the neighborhood pixel in the search window, where the pixel x_j is located with respect to the center x_i, which is $\varepsilon_{ij}=\exp[-(D_j-\overline{D})]$, $j\in W_i^r$. Use the optimization process to find the membership function u_{ki} for Eq. (8), where $\sum_{k=1}^{c}u_{ki}=1$. Then

$$\begin{aligned}&D_1(u_{ti},v_t,\lambda_i)\\&=\sum_{t=1}^{c}u_{ti}^m\left[P(x_i,v_t)+\sum_{j\in W_i^r}\xi_{ij}P(x_j,v_t)\right]\\&+\lambda_i\left(\sum_{t=1}^{c}u_{ti}-1\right).\end{aligned}$$

Thus, the membership of pixel x_i relative to

cluster center v_t is

$$u_{ti}=\left\{\sum_{p=1}^{c}\left[\frac{P\left(x_i,v_t\right)+\sum\limits_{j\in W_i^r}\xi_{ij}P\left(x_j,v_t\right)}{P\left(x_i,v_p\right)+\sum\limits_{j\in W_i^r}\xi_{ij}P\left(x_j,v_p\right)}\right]^{\frac{1}{m-1}}\right\}^{-1}.$$

The update equation of cluster center v_t is as follows:

$$v_t=\frac{\sum\limits_{t=1}^{c}u_{ti}^m\left\{\left(1-P(x_i,v_t)\right)x_i+\sum\limits_{j\in W_i^r}\xi_{ij}\left[\left(1-P\left(x_j,v_t\right)\right)x_j\right]\right\}}{\sum\limits_{t=1}^{c}u_{ti}^m\left[1-P\left(x_i,v_t\right)+\sum\limits_{j\in W_i^r}\xi_{ij}\left(1-P\left(x_j,v_t\right)\right)\right]}.$$

2.3 Obtaining the objective function weight for IRRI segmentation

2.3.1 Model design

Using different weight coefficients to optimize the objective function $f_3(v)$, different solutions can be obtained. The weight coefficient can change the priority of the objective function in $f_3(v)$. Thus, we need to select an appropriate weight vector for the objective functions $f_1(v)$ and $f_2(v)$ to satisfy the IRRI segmentation requirement. Without sufficient prior knowledge, it is difficult to find a satisfactory weight vector and obtain a satisfactory Pareto optimal solution.

For Eq. (3), the optimal compromise solution $(\omega_1^q,\ \omega_2^q)$ is obtained for each IRRI to obtain the optimal defect segmentation result. The segmentation problem is introduced in multi-objective evolution, and the following multi-objective optimization problem is constructed:

$$\begin{aligned}&\min F\left(v\right)=\left[f_1\left(v\right),f_2\left(v\right)\right]^{\mathrm{T}}\\&\text{s.t. }\ v=\left(v_1,v_2,...,v_c\right)^{\mathrm{T}}.\end{aligned}\tag{9}$$

In Eq. (9), c is the number of classifications, and v represents a set of candidate cluster centers. Chebyshev's decomposition technique is used to solve the sub-problems that result from the decomposition of the multi-objective optimization problem (9). The relationship between the weight vector for noise removal and edge information preservation has been updated. The first sub-problem is

$$\begin{aligned}&\min g^{\mathrm{tf}}\left(v\left|\omega^j\right.\right)\\&=\max\left\{\omega_1^j\left|f_1\left(v\right)-f_1^*\right|,\omega_2^j\left|f_2\left(v\right)-f_2^*\right|\right\}.\end{aligned}\tag{10}$$

In Eq. (10), $\omega^j=(\omega_1^j,\ \omega_2^j)$ is the weight vector of the j^{th} sub-problem, and ω_1^j and ω_2^j adjust the degrees of noise cancellation and detail preservation, respectively. Therefore, f_1^* and f_2^* are the current optimal function values for the noise removal and detail preservation functions of impact damage infrared images. A weight vector $\omega^q=(\omega_1^q,\ \omega_2^q)$ corresponding to the Pareto solution closest to the inflection point of Pareto front (PF) is required by Eq. (3).

2.3.2 Model solving algorithm

We use the multi-objective evolutionary algorithm based on decomposition (MOEA/D) to solve the multi-objective optimization problem (9). Based on the idea of decomposition, MOEA/D combines rich mathematical programming with the evolutionary algorithm, and transform the multi-objective optimization problem into a set of single-objective optimization problems. A multi-objective evolutionary algorithm based on decomposition was proposed by Zhang QF and Li (2007). Impressive search performance has been achieved in the literature for various problems (Xing et al., 2017; Zhang X et al., 2017; Tamilselvi et al., 2018). In our preliminary work, Yin et al. (2019) decomposed multi-objective evolutionary algorithms to construct a multi-objective problem of finding representative temperature points with multiple performance considerations for differences and correlations, using the MOEA/D algorithm based on the principle of decomposition. The MOEA/D algorithm's overall solution is as follows: (1) The decomposition algorithm decomposes the problem into several single-objective subproblems with unique weights; (2) The Pareto optimal solution is achieved after a significant number of measurements.

1. Decomposition algorithm

The Tchebycheff algorithm is applied as the core decomposition algorithm in the MOEA/D algorithm (Jaszkiewicz, 2002). Tchebycheff's mathematical expression is as follows:

$$\min g^{\mathrm{te}}\left(x\left|\lambda^j,z^*\right.\right)=\max_{i=1,2,\cdots,m}\left\{\lambda_i^j\left|f_i\left(x\right)-z_i^*\right|\right\}.\tag{11}$$

In Eq. (11), m is the number of objective functions and $g^{\mathrm{te}}\left(x\left|\lambda^j,z^*\right.\right)$ is the sub-objective after decomposition, where $\lambda^j=(\lambda_1^j,\lambda_2^j,...,\lambda_m^j),\sum\limits_{i=1}^{m}\lambda_i^j=1$. $z^*=(z_1^*,z_2^*,...,z_m^*)$ is the reference point and $f_1\left(v\right)$

and $f_2(v)$ both have $z_i^* = \min\{f_i(v) | v \in \Omega\}, \forall i = 1, 2, ..., m$.

2. Evolutionary algorithm

The differential evolution algorithm will increase the ability to search for optimal solution while preserving population diversity in the estimation of the object dilemma. As a result, it is used in the MOEA/D algorithm. The following is the mathematical expression of the differential evolution algorithm:

$$e = \begin{cases} s^{r_0} + \varepsilon(s^{r_1} - s^{r_2}),\ C_R, \\ s^i,\ 1 - C_R, \end{cases} \tag{12}$$

where e is a new individual created as a result of evolution, and C_R ($0 \le C_R \le 1$) and ε are evolutionary control parameters. s^i is the i^{th} individual in the population. r_0, r_1, and r_2 are the actual numbers on the inside.

The IRRI segmentation scheme is as given in Algorithm 1, based on the multi-objective evolutionary theory.

2.3.3 Model solving process

Step 1: parameter setting

The following parameters are set: the objective function of multi-objective optimization in Eq. (12); the maximum iteration number $g_{\max}$; the evolutionary parameters C_R and ε in Eq. (12); the population size N; the number neighborhood weight vectors T.

Step 2: initialization

1. Obtain N weight vectors $\lambda_1, \lambda_2, ..., \lambda_N$ with a uniform distribution and count the T nearest weight vectors of λ^i, denoted as $B(i) = \{i_1, i_2, ..., i_T\}$.

2. This yields an initial population $s^1, s^2, ..., s^N$ that solves the multi-objective problem. Let $\mathrm{FV}^i = F(s^i)$, $i = 1, 2, ..., N$.

3. $z^* = (z_1{}^*, z_2{}^*, ..., z_m{}^*)^{\mathrm{T}}$ is initialized to find the optimal value of the objective function.

4. Set the external population (EP) to the empty set.

Step 3: algorithm update

When the maximum number of iterations has not been reached:

1. Choose k, l from $B(i)$, and use the differential evolution algorithm in Eq. (12) to produce a new solution e from s^k, s^l.

2. The constraint processing proposed in the image segmentation multi-objective optimization problem for e yields e'.

3. Update z: If $z_j < f_j(e')$, then $z_j = f_j(e'), j = 1, 2, ..., m$.

4. Update the neighborhood solution: If $g^{\mathrm{te}}\left(y' \middle| \lambda^j, z\right) \le g^{\mathrm{te}}\left(x^j \middle| \lambda^j, z\right), j \in B(i)$, then $s^j = e'$, $\mathrm{FV}^i = F(e')$ according to Eq. (11).

5. Update EP: Delete all vectors that are occupied by $F(e')$. If $F(e')$ is not governed by vectors in EP, add e' to EP.

Step 4: termination of the iteration

If $g = g_{\max}$ is satisfied, the output EP is optimal; that is, the optimal weight solution $\omega^q = (\omega_1^q, \omega_2^q)$ is obtained for the image segmentation multi-objective problem. Otherwise, $g = g + 1$, and go to step 3. Count the weight vector $\omega^q = (\omega_1^q, \omega_2^q)$, put it into Eq. (3), and obtain the membership function and cluster center. For the following purposes, use the plier method:

$$f_3(v) = \omega_1^q \frac{\sum_{t=1}^{c}\left(\sum_{i=1}^{MN} u_{ti}^m \cdot M(x_i, v_t) \Big/ \sum_{i=1}^{MN} u_{ti}\right)}{\sum_{q=1, q\ne t}^{c} u_{tq}^m \|v_q - v_t\|} + \omega_2^q \sum_{i=1}^{MN}\sum_{t=1}^{c} u_{ti}^m \left[P(x_i, v_t) + \sum_{j\in W_i^r} \xi_{ij}^t P(x_j, v_t)\right]. \tag{13}$$

For Eq. (13), the membership degree update

Algorithm 1 Image segmentation

1: Initialize threshold ε, set the maximum number of iterations T, initialize the cluster center $V^{(1)} = \left(v_1^{(1)}, v_2^{(1)}, ...v_c^{(1)}\right)^{\mathrm{T}}$, and set $h = 1$.

2: Calculate $U^{(h)}$: If $\forall j, p$, $f_3(v) > 0$, then

$$u_{ti}{}^{(h)} = \left\{\sum_{p=1}^{c}\left[\frac{\omega_1^q\left(\Psi_i^{t(h)}\right) + \omega_2^q\left(\Gamma_i^{t(h)}\right)}{\omega_1^q\left(\Psi_i^{p(h)}\right) + \omega_2^q\left(\Gamma_i^{p(h)}\right)}\right]^{\frac{1}{m-1}}\right\}^{-1},$$

where $\Psi_i^{t(h)} = \|x_i - c_t\|^2 + a_1\left\|\delta_i - v_t^{(h)}\right\|^2 + a_2\left\|\tau_i - v_t^{(h)}\right\|^2$, and $\Gamma_i^{t(h)} = P\left(x_i, v_t^{(h)}\right) + \sum_{j\in W_i^r}\xi_{ij}P\left(x_j, v_t^{(h)}\right)$.

3: If $\exists j, p$, $f_3(v) = 0$, then let $u_{pi}{}^{(h)} = 1$ and $t \ne p, u_{ti}{}^{(h)} = 0$.

4: Use Eq. (15) to calculate the cluster center.

5: If $\left\|V^{(h+1)} - V^{(h)}\right\| < \varepsilon$ or $h > T$, the algorithm ends. The optimum segmentation cluster center and the segmentation outcome are obtained; otherwise, $h = h + 1$, and go to step 2.

6: Output E_n.

formula is

$$u_{ti}=\frac{1}{\sum_{p=1}^{c}\left[\frac{\omega_1^q\left(\Psi_i^t\right)+\omega_2^q\left(P(x_i,v_t)+\sum_{j\in W_i^r}\xi_{ij}P(x_j,v_t)\right)}{\omega_1^q\left(\Psi_i^p\right)+\omega_2^q\left(P(x_i,v_p)+\sum_{j\in W_i^r}\xi_{ij}P(x_j,v_p)\right)}\right]^{\frac{1}{m-1}}}, \tag{14}$$

where $\Psi_i^t=\|x_i-c_t\|^2+\beta_1\|\delta_i-c_t\|^2+\beta_2\|\tau_i-c_t\|^2$.

The cluster center update formula is

$$v_t=\frac{\sum_{i=1}^{MN}u_{ti}^m\left[\omega_1^q x_i+\omega_2^q\left(K_i^t x_i+\sum_{j\in W_i^r}\xi_{ij}\left(K_j^t x_j\right)\right)\right]}{\sum_{i=1}^{MN}u_{ti}^m\left[\omega_1^q+\omega_2^q\left(K_i^t+\sum_{j\in W_i^r}\xi_{ij}\left(K_j^t\right)\right)\right]}, \tag{15}$$

where $K_i^t=1-P\left(x_i,v_t\right)$. After obtaining Eqs. (14) and (15), the IRRI can be further divided.

3 IRRI construction algorithm

The IRRI as the segmentation object uses the temperature change characteristics that correspond to different defects in the tested sample to display the defects. We want to use the infrared video stream composed of multiple infrared images to obtain the defect characteristics' characterisation. The specific steps are as the following.

3.1 Step 1: classification of TTRs with the GMM algorithm

1. Infrared video stream sampling

Obtain the initial thermal image sequence of the infrared video stream $S(m,n,\cdot),m=1,2,...,M,n=1,2,...,N$ (Fig. 5), where the three-dimensional matrix has M rows and N columns, and the corresponding frame size is d. Because of the high resolution of thermal images and the number of frames, use a threshold $T(\hat{w})\left(\hat{w}=1,2,...,\hat{h}\right)$ to divide the video stream data into $h+1$ data blocks. Perform TTR collection on the data blocks according to $\mathrm{Re_{cl}}$ and $\mathrm{Re_{row}}$, and vectorize the collected TTRs to obtain a sampled data set $U(\cdot,z_g),g=1,2,...,G$.

2. TTR data set classification

Specify the G TTR curves in $U\left(\cdot,z_G\right)$ as $(x_1,x_2,...,x_G)$, where $x_1=U(\cdot,z_1)$, $x_2=U(\cdot,z_2),\cdots,\ x_G=U(\cdot,z_G)$, and establish a Gaussian mixture probability density function

$$p\left(x_i|\theta^{(v)}\right)=\sum_{k=1}^{K}a_{ik}^v p_k\left(x_i\left|\mu_k^v,\Sigma_k^v\right.\right),\quad \sum_{k=1}^{K}a_{ik}=1,\ i=1,2,...,G, \tag{16}$$

to approximate the complex distribution of the TTRs in the sampled data set, where $p_k\left(x_i\left|\mu_k^v,\Sigma_k^v\right.\right)=\frac{1}{\sqrt{(2\pi)^d\mu_k^v}}\exp\left(-\frac{1}{2}(x_i-\mu_k^v)^{\mathrm{T}}{\Sigma_k^v}^{-1}(x_i-\mu_k^v)\right)$ is the probability density function of the Gaussian distribution. In this study, d is the number of sampling frames in the infrared video stream.

To realize the idea of using the infrared image sequence to obtain IRRI, the transient thermal response curve needs to be measured and classified. Compared with supervised learning (Hou et al., 2020), due to the diversity of defect features, we use prototype clustering to classify TTRs. The disadvantage of using the Euclidean distance metric is the limited maximum zoom, which causes distortion of the distance metric and produces a hyperspherical disk (Fig. 6). Gaussian mixture model (GMM) is a probabilistic model that has advantages in image data classification (Permuter et al., 2006) and noise data classification (Fu et al., 2021). GMM usually assigns data to multivariate normal components for clustering, to maximize the posterior probability of the given data. The fitted model is used to cluster and estimate the posterior probability of the components to obtain the classification results (Reynolds, 2015). In this study, we use GMM to express the characteristic temperature change process as the probability density function of the weighted sum of multiple local Gaussian components. GMM can overcome the limitations of the superelliptical star clusters and normalize continuous features into a common variance range.

3. Find the posterior probability that the i^{th} U comes from the k^{th} Gaussian distribution:

$$\gamma_{ik}{}^{(v)}=p\left(k\left|x_i,\theta^{(v)}\right.\right)=\frac{\left[a_{ik}f_k\left(x_i\left|\mu_k,\Sigma_k\right.\right)\right]^{\partial}}{\left[\sum_{j=1}^{K}a_{ij}f_j\left(x_i\left|\mu_j,\Sigma_j\right.\right)\right]^{\partial}},\quad i=1,2,...,z,\ k=1,2,...,K, \tag{17}$$

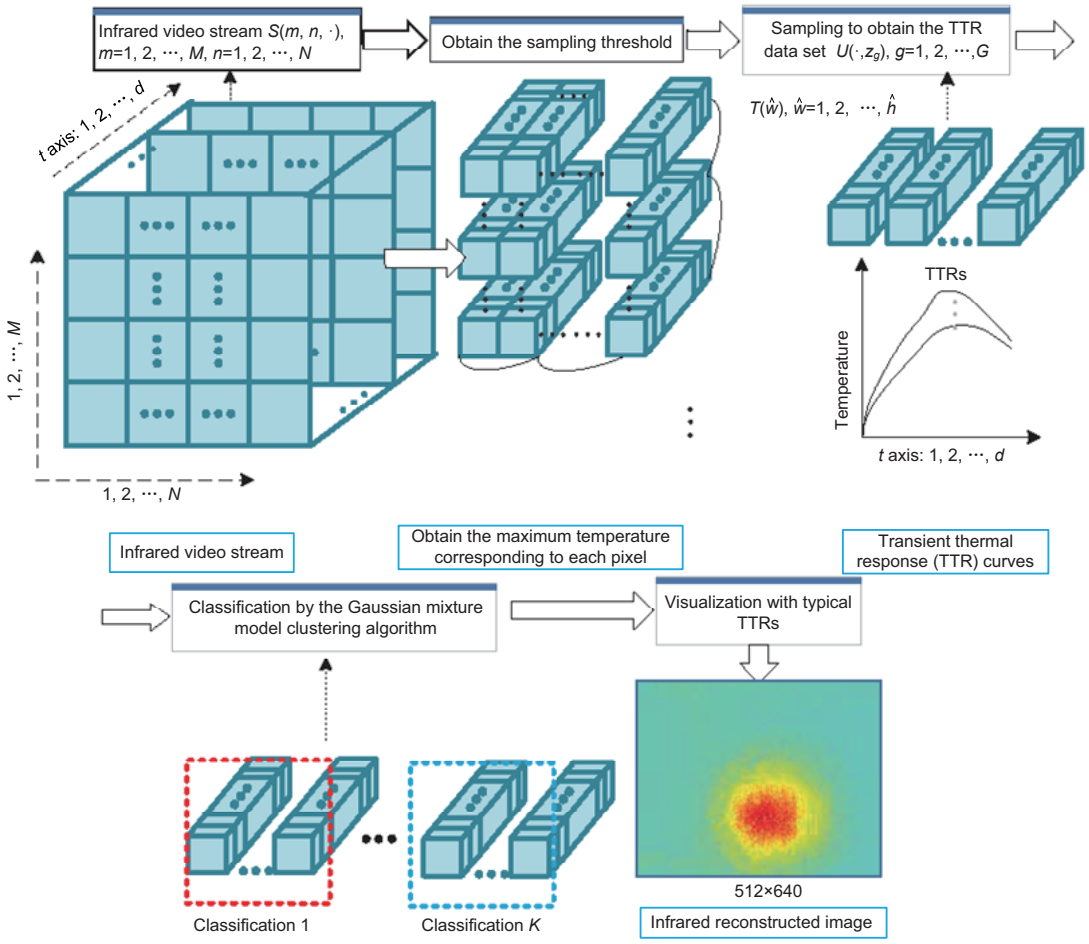

Fig. 5 Schematic of infrared reconstructed image (IRRI) generation

where ∂ is the Lagrangian multiplier, which reduces the influence of the posterior probability in early iterations. First let $\partial = \partial_{\min}, 0 < \partial_{\min} \leq 1$, $v = 0$.

4. We can obtain

$$Q(\theta, \theta^v) = \sum_{k=1}^{K}\sum_{i=1}^{G} p(k\,|x_i, \theta^v) \log a_{ik} + \sum_{k=1}^{K}\sum_{i=1}^{G} p(k\,|x_i, \theta^v) \log p_k(x_i\,|\theta)$$

from $Q(\theta, \theta^v) = E\left[\log p\left(U, Z\,|\theta\right)|U, \theta^v\right]$. Find $\theta^{v+1} = \arg\max_{\theta} Q\left(\theta, \theta^v\right)$; that is, use the following formulae to update the parameters to obtain θ^{v+1}:

Calculate the new mixing factor:

$$a_k^{v+1} = \frac{1}{G}\sum_{i=1}^{G}\gamma_{ik}.$$

Calculate a new mean vector:

$$\mu_k^{v+1} = \sum_{i=1}^{G}\gamma_{ik}x_i \Big/ \sum_{i=1}^{G}\gamma_{ik}.$$

Calculate the new covariance matrix:

$$\Sigma_k^{v+1} = \sum_{i=1}^{G}\gamma_{ik}(x_i - \mu_k)(x_i - \mu_k)^{\mathrm{T}} \Big/ \sum_{i=1}^{G}\gamma_{ik}.$$

5. Increase ∂. If the stop condition $\partial > 1$ is met, the iteration stops and the GMM model parameters are output; otherwise, go to steps 2–4.

6. Use the final model parameters to solve Eq. (16) to divide the G TTRs in the sample set U into K clusters using Eq. (17). The x_i label of each sample is counted by the following formula: $k = \arg\max_{k\in\{1,2,\ldots,K\}} \gamma_{ik}, k = 1, 2, \ldots, K$. Divide x_i into the corresponding cluster $D_k = D_k \cup \{x_i\}$, and divide the TTRs into clusters $D = \{D_1, D_2, \ldots, D_K\}$;

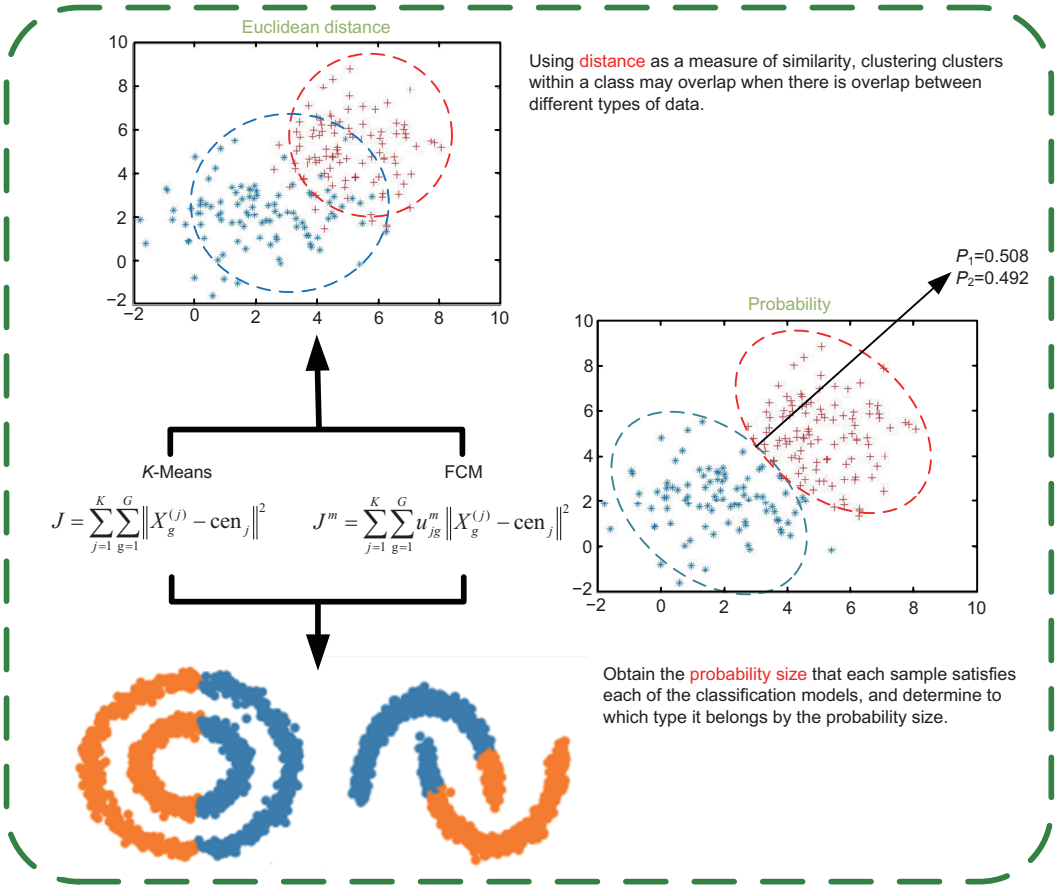

Fig. 6 Schematic of the difference between Euclidean distance and Gaussian probability density function clustering

that is, divide the TTRs in the sample set into K types.

7. Select the cluster that corresponds to the maximum posterior probability $\text{RE}^k = \max w_{ik}$, $k = 1, 2, ..., K$ in each cluster of D as the K most representative TTRs, which are stored in matrix $H_1(\cdot, k)$, $k = 1, 2, ..., K$.

3.2 Step 2: obtaining IRRI using typical thermal response curves

The process is shown in Table 1. The schematic of the IRRI extraction algorithm described in this subsection is shown in Fig. 5. Different defects have different temperature change characteristics. In this subsection, the GMM algorithm is used to classify the TTRs in the infrared image sequence and extract the typical TTR. The typical TTR obtained is reconstructed to obtain the IRRI.

Table 1 Step 2 for the IRRI segmentation algorithm

$S(m, n, \cdot) \Rightarrow P(x, y)_{a\times b}, a = d, b = M \times N$
$O = \hat{H}_1' * P$
$\hat{H}_1'$ is the pseudo-inverse matrix of matrix H_1
$O_{K\times MN} \Rightarrow K$ IRRIs of size $M \times N$ are obtained

4 Experiments

A sample from an ultra-high-speed impact test of an aerospace material composite metal plate was used in the experiments. A certain number of perforation defects and impact stress areas were generated in the sample due to the hypervelocity impact, but they cannot be clearly distinguished.

The infrared thermal spectrum was used to record the thermal distribution on the surface of the test specimen excited by a halogen lamp with infrared resolution of 512 × 640 for infrared thermal video acquisition. For sample A we received 502 frames of size 512 × 640 pixels. The experimental platform was Windows 10, Intel® Core™ i5-4260U

CPU@1.40 GHz, 16 GB memory, MATLAB 2017b.

4.1 Obtaining IRRI

We set the number of classifications K to 3. In this experiment, $U(\cdot, z_g)$ $(g = 1, 2, ..., 502)$ were obtained for $S(m, n, \cdot)_{512\times640\times502}$. According to Section 3, the TTRs were classified using the GMM algorithm. The parameters are shown in Table 2. The probability that the TTRs correspond to the classification model for the corresponding classification were calculated (Table 3).

Table 2 GMM parameters for the sample

Parameter	Value
GMM related	$p(x\,\|\theta) = w_i f_i(x\,|\mu_i, \Sigma_i), i = 1, 2, 3$ $w_1 = 0.2669, w_2 = 0.1486, w_3 = 0.5846$
μ	$\mu_1 = [\ 27.292 \quad 27.347 \quad \cdots \quad 29.214\ ]_{1\times502}$ $\mu_2 = [\ 27.335 \quad 27.461 \quad \cdots \quad 29.214\ ]_{1\times502}$ $\mu_3 = [\ 28.059 \quad 28.064 \quad \cdots \quad 30.730\ ]_{1\times502}$
Σ	$\Sigma_1 = \begin{bmatrix} 0.0460 & 0.0471 & \cdots \\ 0.0471 & 0.0509 & \cdots \\ \vdots & \vdots & \end{bmatrix}_{502\times502}$ $\Sigma_2 = \begin{bmatrix} 0.0912 & 0.1025 & \cdots \\ 0.1025 & 0.1204 & \cdots \\ \vdots & \vdots & \end{bmatrix}_{502\times502}$ $\Sigma_3 = \begin{bmatrix} 1.0771 & 1.0657 & \cdots \\ 1.0657 & 1.0562 & \cdots \\ \vdots & \vdots & \end{bmatrix}_{502\times502}$

Table 3 Video stream data classification by GMM

Data type	Value
Original TTRs	327 680
Sampling TTRs	$G = 727$
Classification	$C_1^{\text{gmm}} = 93$ $C_2^{\text{gmm}} = 74$ $C_3^{\text{gmm}} = 49$ $C_1^{\text{fcm}} = 50^*$ $C_2^{\text{fcm}} = 198^*$ $C_3^{\text{fcm}} = 498^*$

*The number of repetitions is 7

As shown in Figs. 7 and 8, the same sampled data set was processed using FCM and GMM, separately. It can be seen from Fig. 7 that there were repeated classification data with membership degrees $P_1 = P_2 = P_3 = 0.333$. As shown in Fig. 8, two points corresponding to a TTR were extracted, and their temperature change rates were similar. It can be concluded that the GMM algorithm used in this study has good classification performance on the data set, to ensure that the reconstructed image can correctly reflect the defect characteristics.

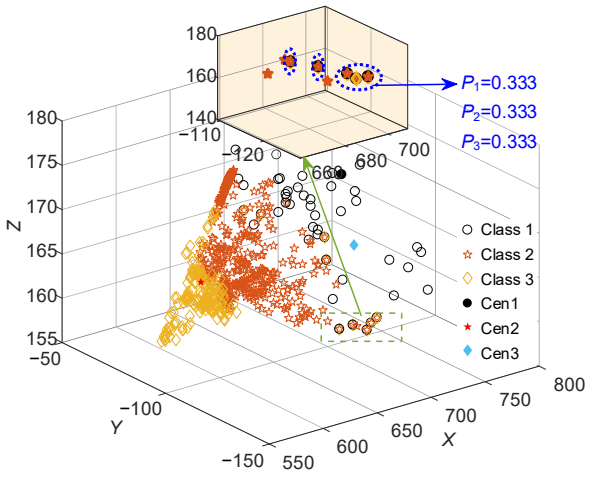

Fig. 7 FCM classification results for the sample (References to color refer to the online version of this figure)

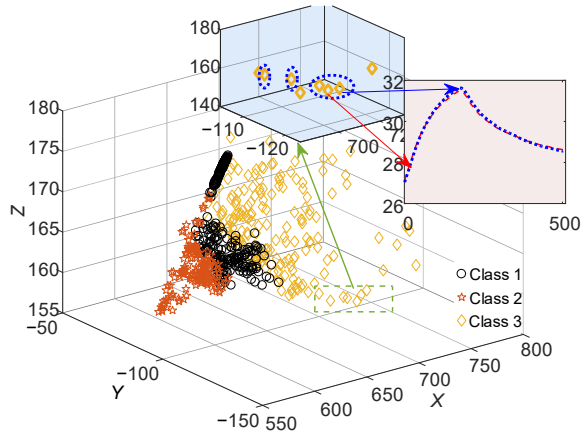

Fig. 8 GMM classification results for the sample (References to color refer to the online version of this figure)

Using the steps shown in Table 4 we obtained three IRRIs, and the corresponding TTR curves are shown in Fig. 9.

Table 4 Obtaining IRRI using a linear matrix

$S(m, n, \cdot) \Rightarrow P(x, y)_{a\times b}, a = 502, b = 327\,680$
$O = \hat{H}_1 * P$
$\hat{H}_1'$ is the pseudo-inverse matrix of matrix H_1
$O_{3\times327\,680} \Rightarrow$ Three IRRIs are obtained

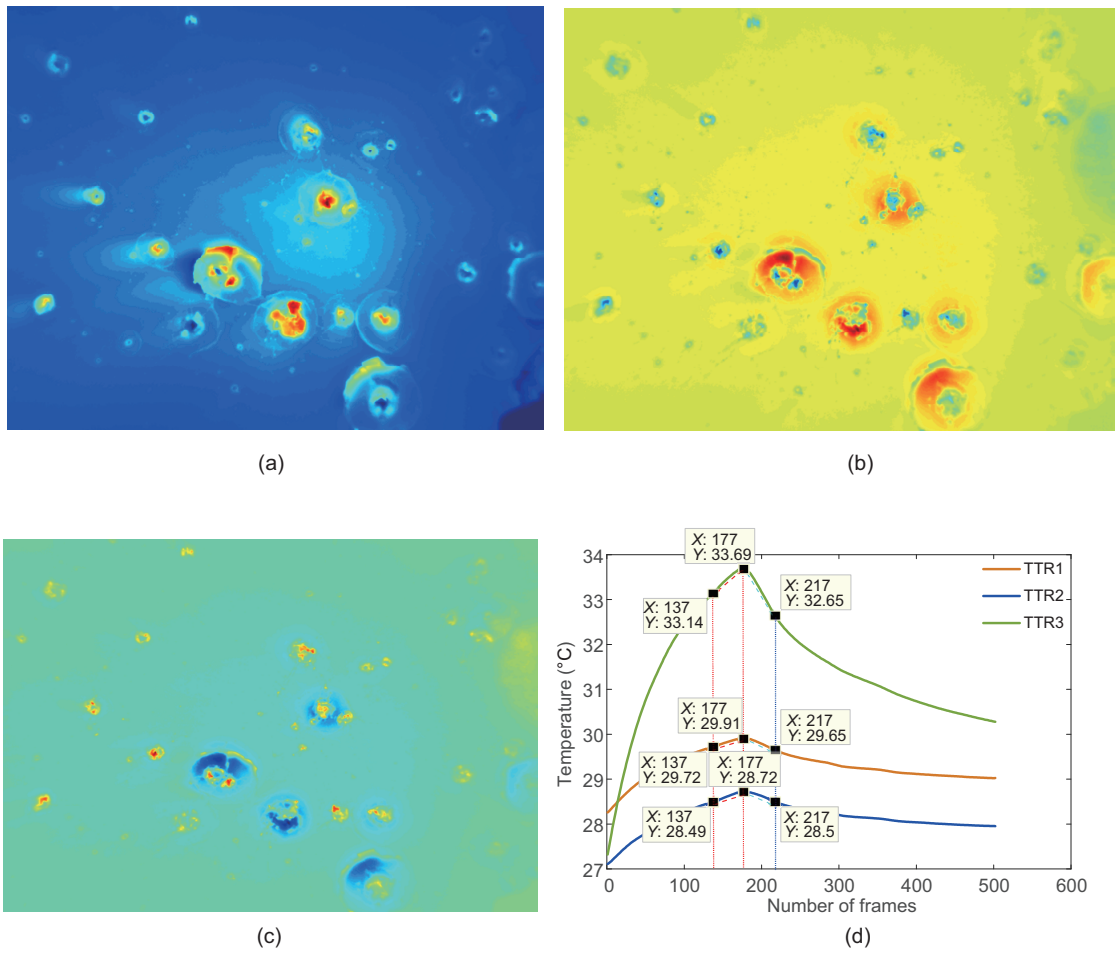

Fig. 9 IRRI acquisition results for the sample: (a) stress damage around the perforation defect; (b) drum kit; (c) perforation damage; (d) TTR for damage (References to color refer to the online version of this figure)

1. Stress damage around the perforation defect

Stress damage was created when the impact energy worked on the periphery of the perforation defect during internal penetration. High average thermal resistance was caused by uneven defect thickness, the heating rate was higher, and the temperature peak was 29.91 °C; the cooling rate was first high and was then affected by the lower area. The cooling rate gradually decreased.

2. Drum kit

Due to the high overall thermal resistance of the defect and faster heat exchange with the air, the temperature showed a slow rise during the heating process, and the peak point was low.

3. Perforation defects

For fragments generated by hypervelocity impacts, the largest impact fragments or scattered, uniformly sized impact fragments can cause damage. According to the TTR curve, it can be seen that the perforation part directly transmitted heat to the infrared thermal imager, which showed the characteristics of faster heating and cooling.

4.2 IRRI segmentation

The algorithm proposed in this study aims to segment Fig. 10 to help identify and quantify defects later. The parameters involved in the algorithm are shown in Table 5.

Our algorithm first evaluated Eq. (9), used the MOEA/D algorithm to obtain the weight vector (ω_1^q=0.6721, ω_2^q=0.3279), and substituted it into Eq. (3), which obviously changed the corresponding weight coefficients in Eq. (3). The MOEA/D algorithm was used to solve the multi-objective optimization problem, and the PF surface formed by the PF solution and the spatial Pareto

optimization set was finally obtained (Fig. 11). Then the cluster centers corresponding to the inflection points in the PF curve were used to segment the IRRI. For $f_1(v)$, the intermediate parameter L-Info $\delta_i = [7.4594,\ 7.4596,\ ...]^{\mathrm{T}}_{327\,680\times1}$ and NL-Info $\tau_i = [0.9276,\ 0.9455,\ ...]^{\mathrm{T}}_{327\,680\times1}$ were obtained. For $f_2(v)$, in the weighted fuzzy factor $\xi^t_{ij} = \zeta_{\mathrm{dc}} \cdot \zeta_{\mathrm{gc}} \cdot (1-u_{tj})^m$, where $\zeta_{\mathrm{dc}} = [2.1248,\ 2.1254,\ ...]^{\mathrm{T}}_{327\,680\times1}$, $\zeta_{\mathrm{gc}}=\begin{bmatrix} 1.4142 & \cdots \\ \cdots & \cdots \end{bmatrix}_{8\times327\,680}$. The MOEA/D algorithm was used to solve the multi-objective optimization problem to finally obtain the PF solution and the formed PF (Fig. 11).

In the dual process embodied here, first a trade-off solution was selected. Then the trade-off solution was used to obtain the optimal solution of $f_3(v)$. Changing the corresponding weight coefficient can change the priority of the objective function and optimize the segmentation problem, so that we can obtain a set of PF solutions. Then the segmented image corresponding to the cluster center [14.420, 1.282, −17.572, 2.685, 0.892, 0.489] in the inflection point in the PF solution was used for segmentation.

Table 5 Multi-objective optimization segmentation algorithm parameters

Parameter	Value
Maximum number of iterations, $g_{\max}$	100
Fuzzy index, m	2
Population, N	30
Number of clusters, c	2
DEPF $f_1(v)$ parameter, r	3
NOSF $f_2(v)$ parameter $s(s,\psi)$	(5, 30)
Number of groups of weight vectors, T	40

We verified the effect of the different objective segmentation functions of the proposed algorithm on the segmented image through the combination of weights. The segmentation results obtained by each sub-target segmentation function $f_1(v)$ or $f_2(v)$ constructed in this study are presented in Fig. 12.

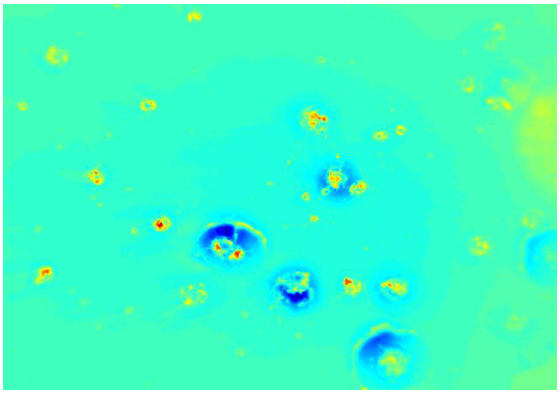

Fig. 10 IRRI to be segmented (References to color refer to the online version of this figure)

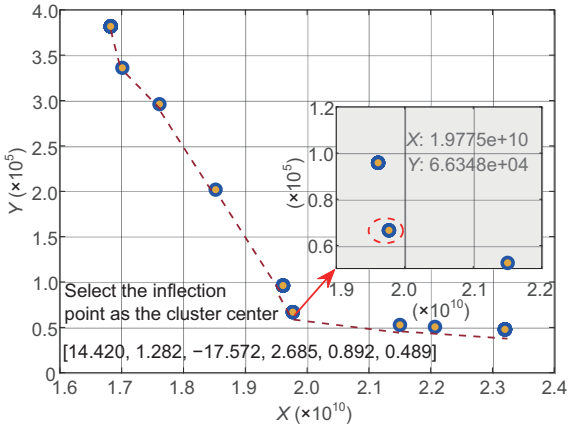

Fig. 11 Pareto front

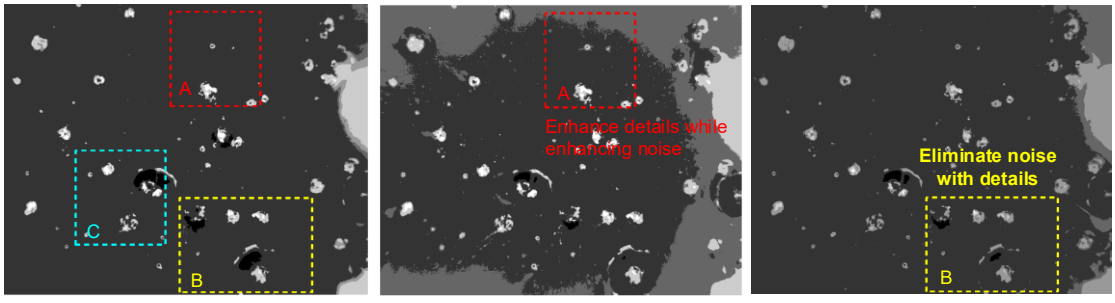

(a) (b) (c)

Fig. 12 Comparison of the image segmentation results of our proposed algorithm with those of the single segmentation function involved in the algorithm: (a) image segmentation object in this study; (b) detail preservation function (DEPF) $f_1(v)$ segmentation result; (c) noise suppression function (NOSF) $f_2(v)$ segmentation result (References to color refer to the online version of this figure)

Fig. 12b shows that the detailed information of the segmented image under the DEPF $f_1(v)$ was retained. It can be seen that the clustering results contained many noise points. In contrast, comparing area B in Figs. 12a and 12c, it can be seen that in Fig. 12c, under the effect of $f_2(v)$, the noise of the segmented image had better suppression effect. However, some defect details such as stress damage and perforation damage around the perforation defect were also suppressed. The weight combination of ω_1^q and ω_2^q was used to obtain the segmentation results with complete detail preservation and less noise. It can be seen that the IRRI segmentation based on a single performance function cannot achieve the desired effect, which verifies the necessity of our algorithm to introduce a multi-objective optimization framework.

To emphasize the effectiveness of the proposed algorithm, we conducted a more detailed analysis through theory and experiments. We compared it with the following four traditional algorithms: FCM_S (Ahmed et al., 1999), FLICM (Krinidis and Chatzis, 2010), fast and robust fuzzy C-means (FRFCM) (Lei et al., 2018), and deviation-sparse fuzzy C-means (DSFCM) (Zhang YX et al., 2019). The codes of these four algorithms are open-source ones, and the parameters were set to their default values. The images used in the comparison experiments are shown in Fig. 13 in terms of the different sized damages caused by the impact on the test object. It can be seen that the FCM_S algorithm had the roughest segmentation results. The segmentation threshold of the algorithm is a soft threshold, which improves the anti-noise ability of the FCM segmentation algorithm, but it is still prone to incomplete segmentation. When segmenting the area of concentrated defect pixels, the defect details are treated as noise. For images with more details such as IRRIs, the FCM_S algorithm cannot achieve correct and effective segmentation. As shown in the Figs. 13c and 13d, the results of DSFCM and FLICM IRRI processing were similar. They usually cannot effectively distinguish relatively scattered target areas, and can divide only larger concentrated areas. Among them, the FLICM algorithm cannot accurately segment the edges of perforation and stress damage with gray-scale approximation because they do not consider the positional relationship or gray-scale

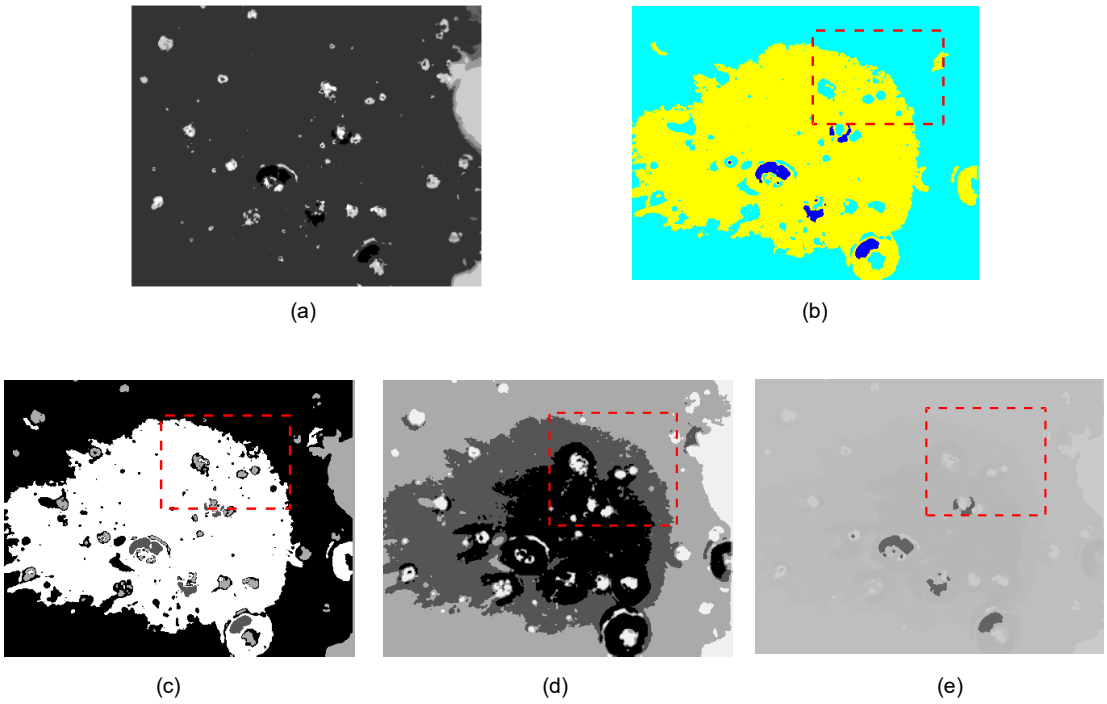

Fig. 13 Comparison of the segmentation results of the proposed algorithm and four state-of-the-art segmentation algorithms: (a) image segmentation object in this study; (b) FCM_S segmentation result; (c) FLICM segmentation result; (d) DSFCM segmentation result; (e) FRFCM segmentation result (References to color refer to the online version of this figure)

relationship between pixels. The DSFCM algorithm had a better processing effect on noise while considering the pixel neighborhood relationship, but it cannot handle the detailed features of the IRRI well, and the segmentation was not accurate. In the segmentation processing of small parts (that is, tiny impact craters), these algorithms usually cannot effectively deal with weak edges. As shown in Fig. 13e, FRFCM was simple and fast, and it also had a good effect on dealing with IRRI noise. However, when the FRFCM algorithm was used for the perforated area and the non-perforated area of the defect, it is very unreasonable for the FRFCM algorithm to simultaneously divide the two areas directly. In this study, we propose an improved algorithm to avoid this situation. Our algorithm can effectively distinguish the target part (perforated and non-perforated areas) in the detailed area, divide it correctly, and produce a clear result of dividing the defect edge. The results in Fig. 13a showed that the improved algorithm can accurately separate perforated and non-perforated areas, stress damage, background, and other parts, and that the image obtained after segmentation was closer to the original image.

5 Conclusions

We designed a defect detection algorithm using infrared video streams to detect defects in spacecraft specimens impacted at hypervelocity. First, we obtained the infrared reconstructed image (IRRI) that highlights different defect features using GMM to extract different temperature change information, that is, transient thermal responses. To separate the damaged part from the background, and to avoid the possible noise interference and blurring of details in IRRI, an adapted objective segmentation function was designed. To obtain more accurate segmentation, we used the idea in solving multi-objective optimization problems to obtain segmentation weights that adapt to each IRRI by constructing a two-layer multi-objective optimization segmentation algorithm. Experimental results verified the effectiveness of the algorithm.

Contributors

Xiao YANG and Chun YIN designed the research and processed the data. Xiao YANG drafted the paper. Chun YIN helped organize the paper. Sara DADRAS, Guangyu LEI, and Xutong TAN helped revise the paper. Xiao YANG, Chun YIN, and Gen QIU finalized the paper.

Compliance with ethics guidelines

Xiao YANG, Chun YIN, Sara DADRAS, Guangyu LEI, Xutong TAN, and Gen QIU declare that they have no conflict of interest.

References

Adushkin VV, Aksenov OY, Veniaminov SS, et al., 2020. The small orbital debris population and its impact on space activities and ecological safety. *Acta Astronaut*, 176:591-597. https://doi.org/10.1016/j.actaastro.2020.01.015

Aglietti GS, Taylor B, Fellowes S, et al., 2020. The active space debris removal mission removedebris. Part 2: in orbit operations. *Acta Astronaut*, 168:310-322. https://doi.org/10.1016/j.actaastro.2019.09.001

Ahmed MN, Yamany SM, Farag AA, et al., 1999. Bias field estimation and adaptive segmentation of MRI data using a modified fuzzy C-means algorithm. Proc IEEE Computer Society Conf on Computer Vision and Pattern Recognition, p.250-255. https://doi.org/10.1109/CVPR.1999.786947

Bandyopadhyay S, Maulik U, Mukhopadhyay A, 2007. Multiobjective genetic clustering for pixel classification in remote sensing imagery. *IEEE Trans Geosci Remote Sens*, 45(5):1506-1511. https://doi.org/10.1109/TGRS.2007.892604

Biju VG, Mythili P, 2015. Fuzzy clustering algorithms for cDNA microarray image spots segmentation. *Proc Comput Sci*, 46:417-424. https://doi.org/10.1016/j.procs.2015.02.039

Bossi RH, Georgeson GE, 2018. Nondestructive testing of composites. *Mater Eval*, 76(8):1048.

Cheng YH, Tian LL, Yin C, et al., 2018. Research on crack detection applications of improved PCNN algorithm in MOI nondestructive test method. *Neurocomputing*, 277:249-259. https://doi.org/10.1016/j.neucom.2017.02.099

Ciampa F, Mahmoodi P, Pinto F, et al., 2018. Recent advances in active infrared thermography for non-destructive testing of aerospace components. *Sensors*, 18(2):609. https://doi.org/10.3390/s18020609

Florez-Ospina JF, Benitez HD, 2014. From local to global analysis of defect detectability in infrared non-destructive testing. *Infrared Phys Technol*, 63:211-221. https://doi.org/10.1016/j.infrared.2013.12.017

Fu YL, Liu XN, Sarkar S, et al., 2021. Gaussian mixture model with feature selection: an embedded approach. *Comput Ind Eng*, 152:107000. https://doi.org/10.1016/j.cie.2020.107000

Garnier C, Pastor ML, Eyma F, et al., 2011. The detection of aeronautical defects in situ composite structures using non destructive testing. *Comp Struct*, 93(5):1328-1336. https://doi.org/10.1016/j.compstruct.2010.10.017

Gharnali B, Alipour S, 2018. MRI image segmentation using conditional spatial FCM based on kernel-induced distance measure. *Eng Technol Appl Sci Res*, 8(3):2985-2990. https://doi.org/10.48084/etasr.1999

Gurtin ME, Francis EC, 1981. Simple rate-independent model for damage. *J Spacecr Rock*, 18(3):285-286. https://doi.org/10.2514/3.57817

Hossain MD, Chen DM, 2019. Segmentation for object-based image analysis (OBIA): a review of algorithms and challenges from remote sensing perspective. *ISPRS J Photogr Remote Sens*, 150:115-134. https://doi.org/10.1016/j.isprsjprs.2019.02.009

Hou L, Luo XY, Wang ZY, et al., 2020. Representation learning via a semi-supervised stacked distance autoencoder for image classification. *Front Inform Technol Electron Eng*, 21(7):1005-1018. https://doi.org/10.1631/FITEE.1900116

Huang XG, Yin C, Ru HQ, et al., 2020. Hypervelocity impact damage behavior of B_4C/Al composite for MMOD shielding application. *Mater Des*, 186:108323. https://doi.org/10.1016/j.matdes.2019.108323

Jaszkiewicz A, 2002. On the performance of multiple-objective genetic local search on the 0/1 knapsack problem—a comparative experiment. *IEEE Trans Evol Comput*, 6(4):402-412. https://doi.org/10.1109/TEVC.2002.802873

Krinidis S, Chatzis V, 2010. A robust fuzzy local information C-means clustering algorithm. *IEEE Trans Image Process*, 19(5):1328-1337. https://doi.org/10.1109/TIP.2010.2040763

Lamb H, 2018. Space agencies turn focus on small space debris. *Eng Technol*, 13(1):48-49. https://doi.org/10.1049/et.2018.0104

Lei T, Jia XH, Zhang YN, et al., 2018. Significantly fast and robust fuzzy C-means clustering algorithm based on morphological reconstruction and membership filtering. *IEEE Trans Fuzzy Syst*, 26(5):3027-3041. https://doi.org/10.1109/TFUZZ.2018.2796074

Liu ML, Lissenden CJ, Wang Q, et al., 2017. Characterization of damage in shielding structures of space vehicles under hypervelocity impact. *Proc Eng*, 188:286-292. https://doi.org/10.1016/j.proeng.2017.04.486

Maldague XP, 2001. Theory and Practice of Infrared Technology for Nondestructive Testing. John Wiley & Sons, New York, USA, p.307.

Maulik U, Sarkar A, 2012. Efficient parallel algorithm for pixel classification in remote sensing imagery. *Geoinformatica*, 16(2):391-407. https://doi.org/10.1007/s10707-011-0136-5

Meola C, Boccardi S, Carlomagno GM, et al., 2015. Nondestructive evaluation of carbon fibre reinforced composites with infrared thermography and ultrasonics. *Comp Struct*, 134:845-853. https://doi.org/10.1016/j.compstruct.2015.08.119

Murtaza A, Pirzada SJH, Xu TG, et al., 2020. Orbital debris threat for space sustainability and way forward. *IEEE Access*, 8:61000-61019. https://doi.org/10.1109/ACCESS.2020.2979505

Namburu A, Samayamantula SK, Edara SR, 2017. Generalised rough intuitionistic fuzzy C-means for magnetic resonance brain image segmentation. *IET Image Process*, 11(9):777-785. https://doi.org/10.1049/iet-ipr.2016.0891

Permuter H, Francos J, Jermyn I, 2006. A study of Gaussian mixture models of color and texture features for image classification and segmentation. *Patt Recogn*, 39(4):695-706. https://doi.org/10.1016/j.patcog.2005.10.028

Reynolds D, 2015. Gaussian mixture models. In: Li SZ, Jain A (Eds.), Encyclopedia of Biometrics (2nd Ed.). Springer, Boston. https://doi.org/10.1007/978-1-4899-7488-4_196

Schonberg WP, 2009. Assessing the resiliency of composite structural systems and materials used in Earth-orbiting spacecraft to hypervelocity projectile impact. In: Hiermaier S (Ed.), Predictive Modeling of Dynamic Processes: a tribute to Professor Klaus Thoma. Springer, Boston, p.397-416. https://doi.org/10.1007/978-1-4419-0727-1_21

Tamilselvi S, Baskar S, Anandapadmanaban L, et al., 2018. Multi objective evolutionary algorithm for designing energy efficient distribution transformers. *Swarm Evol Comput*, 42:109-124. https://doi.org/10.1016/j.swevo.2018.01.007

Vaibhavi P, Rupal K, 2018. Brain tumor segmentation using K-means-FCM hybrid technique. In: Perez GM, Tiwari S, Trivedi MC, et al. (Eds.), Ambient Communications and Computer Systems. Springer, Singapore, p.341-352. https://doi.org/10.1007/978-981-10-7386-1_30

Veidt M, Liew CK, 2013. 17-non-destructive evaluation (NDE) of aerospace composites: structural health monitoring of aerospace structures using guided wave ultrasonics. In: Karbhari VM (Ed.), Non-destructive Evaluation (NDE) of Polymer Matrix Composites: Techniques and Applications. Woodhead Pub, Philadelphia, USA, p.449-479. https://doi.org/10.1533/9780857093554.3.449

Wu ZD, Xie WX, Yu JP, 2003. Fuzzy C-means clustering algorithm based on kernel method. Proc 5th Int Conf on Computational Intelligence and Multimedia Applications, p.49-54. https://doi.org/10.1109/ICCIMA.2003.1238099

Xie XL, Beni G, 1991. A validity measure for fuzzy clustering. *IEEE Trans Patt Anal Mach Intell*, 13(8):841-847. https://doi.org/10.1109/34.85677

Xing HL, Wang ZY, Li TR, et al., 2017. An improved MOEA/D algorithm for multi-objective multicast routing with network coding. *Appl Soft Comput*, 59:88-103. https://doi.org/10.1016/j.asoc.2017.05.033

Xu L, Huang G, Chen QL, et al., 2020. An improved method for image denoising based on fractional-order integration. *Front Inform Technol Electron Eng*, 21(10):1485-1493. https://doi.org/10.1631/FITEE.1900727

Yin C, Xue T, Huang XG, et al., 2019. Research on damages evaluation method with multi-objective feature extraction optimization scheme for M/OD impact risk assessment. *IEEE Access*, 7:98530-98545. https://doi.org/10.1109/ACCESS.2019.2930114

Zhang QF, Li H, 2007. MOEA/D: a multiobjective evolutionary algorithm based on decomposition. *IEEE Trans Evol Comput*, 11(6):712-731. https://doi.org/10.1109/TEVC.2007.892759

Zhang X, Zhou Y, Zhang QF, et al., 2017. Problem specific MOEA/D for barrier coverage with wireless sensors. *IEEE Trans Cybern*, 47(11):3854-3865. https://doi.org/10.1109/TCYB.2016.2585745

Zhang YX, Bai XZ, Fan RR, et al., 2019. Deviation-sparse fuzzy C-means with neighbor information constraint. *IEEE Trans Fuzzy Syst*, 27(1):185-199. https://doi.org/10.1109/TFUZZ.2018.2883033